

In-situ reconstructed In doped SnO₂ amorphous–crystalline heterostructure for highly efficient CO₂ electroreduction with a dynamic structure–function relationship

Fei Liu ^a, Jiajun Wang ^{a,*}, Xixi Ren ^a, Han Wu ^a, Jun Zhao ^a, Jinfeng Zhang ^a, Wei Xie ^d, Guangjin Wang ^e, Xiaopeng Han ^{a,*}, Yida Deng ^{a,b,**}, Wenbin Hu ^{a,c}

^a Key Laboratory of Advanced Ceramics and Machining Technology of Ministry of Education, School of Materials Science and Engineering, Tianjin University, Tianjin 300072, PR China

^b State Key Laboratory of Marine Resource Utilization in South China Sea, School of Materials Science and Engineering, Hainan University, Haikou 570228, PR China

^c Joint School of National University of Singapore and Tianjin University, International Campus of Tianjin University, Binhai New City, Fuzhou 350207, PR China

^d Key Lab of Advanced Energy Materials Chemistry (Ministry of Education), Tianjin Key Lab of Biosensing & Molecular Recognition, Haihe Laboratory of Sustainable Chemical Transformations, Renewable Energy Conversion and Storage Center College of Chemistry, Nankai University, Tianjin 300071, PR China

^e School of Materials Science and Hydrogen Energy, Foshan University, Foshan 528000, PR China

ARTICLE INFO

Keywords:

CO₂ electroreduction
In-situ reconstruction
Amorphous–crystalline heterostructure
Dynamic structure–function relationship
Catalytic mechanism

ABSTRACT

While amorphous metal oxides exhibit potential advantages in terms of energy conversion and storage, they undergo unavoidable and uncontrollable reconstruction during electrocatalysis. Monitoring the probable reconstruction of catalytic materials during operation is crucial for identifying the practical active sites. In this study, the amorphous In-doped SnO_x (a-In-SnO_x) was selected for the in-situ reconstruction of highly active structures. In/ex-situ electron microscopy revealed that the intricate reconstruction of a-In-SnO_x could be divided into three states: initial, activated, and deactivated. The a-In-SnO_x reconstructed amorphous–crystalline In-doped SnO₂ heterostructure for highly efficient CO₂ electroreduction. Benefiting from the heterostructure, the amorphous-crystalline In-doped SnO₂ (a/c-In-SnO₂) exhibited potential CO₂RR performance with a maximum Faraday efficiency of 94.6% at -1.0 V (vs. RHE) and a current density of 209 mA cm⁻² at -1.4 V (vs. RHE). This work represents significant advancements in design of active amorphous–crystalline heterostructures during the reconstruction process and establishes a dynamic evolution mechanism.

1. Introduction

Using renewable electric power to drive CO₂ electrochemical reduction to high-value-added chemical fuels can address the issue of severely increasing carbon dioxide emissions and achieve direct conversion of intermittent electrical energy to chemical energy—a sustainable strategy for controlling carbon balance and optimising the energy consumption structure [1–3]. Formic acid (HCOOH), one of the CO₂ electrochemical reduction reaction (CO₂RR) products, has several industrial uses because of its high energy density and ease of transportation. With its moderate circumstances and excellent energy-input efficiency, the electrocatalytic CO₂RR→HCOOH is considered a potential CO₂ conversion method. In recent years, various electrocatalysts

(such as Cu, Ag, Bi, In, and Sn) have been used for the CO₂RR [4–6]. Owing to their low cost, environmental friendliness, and high selectivities for formic acid, SnO₂-based catalysts are most likely to be applied in the CO₂RR field on a large scale [7]. Consequently, various strategies, such as heteroatom doping [8,9], defect engineering [10,11], and carbon composition [12], have been developed to regulate the exposed active sites and enhance the charge-transfer rate to promote the activity of the CO₂RR. For example, Lei et al. reports that In atom doping can regulate the electronic structure of SnO₂, improving the electrical conductivity, regulating the oxidation state of Sn active sites, and providing more active sites [13]. Recently, Chang et al. prepare bimetallic In–Sn nanoparticles (NPs) with unique core–shell structures. Owing to the uniformly dispersed In–Sn hybrid core and native Sn-doped In₂O₃ shell,

* Corresponding authors.

** Corresponding author at: State Key Laboratory of Marine Resource Utilization in South China Sea, School of Materials Science and Engineering, Hainan University, Haikou 570228, PR China.

E-mail addresses: wangjiajun90@tju.edu.cn (J. Wang), xphan@tju.edu.cn (X. Han), yd_deng@hainanu.edu.cn (Y. Deng).

In-Sn NPs exhibit more active In-Sn bimetallic interfaces. Moreover, adjusting the elemental composition significantly enhance the yield of CO₂ reduction to formate over a wide potential window compared to pure single-metal counterparts. Their research demonstrate that In can be used as an auxiliary element to enhance the CO₂RR performance of SnO₂ [14]. Notably, electrochemical reconstruction generally occurs in SnO₂-based materials during CO₂RR. For instance, Ning et al. demonstrate that SnO₂ undergoes a reconstruction process and exhibits excellent electrocatalytic activity towards CO₂RR owing to the reconstruction into SnO₂/Sn heterojunctions during CO₂RR electrolysis [15]. Therefore, utilizing reconstruction to in-situ generate high active sites is an attractive strategy for designing SnO₂-based catalysts. However, the electrochemical performance of the above materials cannot satisfy industrialized application. Moreover, the material reconstruction process and the actual active structure in the catalytic process still need to be further explored. The combination of multiple in situ characterizations and theoretical calculations for further investigate relevant catalytic mechanisms is scarce. Therefore, it is necessary to adopt new research perspectives and material systems to improve the performance of SnO_x-based materials and deepen the understanding of their catalytic mechanisms.

Non-precious amorphous metal oxides exhibit multifunctional activities across electrocatalytic fields for energy conversion and storage [16]. Owing to their defect structures, high corrosion resistance, and extra active sites, amorphous metal oxides exhibit excellent electrochemical performance, highlighting their potential applications in water-splitting reactions, metal-air batteries, and low-power fuel cells [17,18]. Therefore, constructing amorphous-crystalline heterostructures can effectively increase the number of active sites. In contrast to conventional crystalline heterostructures, amorphous-crystalline heterostructures can regulate the electronic structure over a much larger range owing to the disordered arrangement of amorphous atoms [19, 20], regulating more active sites to participate in the CO₂RR. However, research on the in-situ reconstruction of highly active amorphous-crystalline heterostructures from amorphous oxide materials remains limited. Moreover, owing to the inevitable reconstruction during operation, the structure of the reconstructed material is different from its initial state under electrolytic conditions [21–23]. Therefore, there is an urgent need to systematically establish the dynamic structure–function relationship for in-situ electrochemically formed amorphous-crystalline structures. Moreover, using amorphous metal oxides as models to explore the reconstruction behaviour and dynamic structure–function relationship is imperative for the precise identification of active sites, further understanding of the catalytic mechanisms, and rational design of CO₂RR catalysts.

In this study, we developed amorphous In-doped SnO_x (a-In-SnO_x) as a basic material for the in-situ reconstruction of highly active structures via electrochemical activation. A series of ex/in-situ characterisations and density functional theory (DFT) calculations were used to monitor the reconstruction process and explore the real active sites under electrocatalytic conditions for the CO₂RR. We found that the a-In-SnO_x could transform into amorphous In-doped SnO_x/In-doped SnO₂ heterostructures during operation, facilitating excellent electrocatalytic performance for the CO₂RR. Moreover, we proposed a three-state description (initial, activated, and deactivated states) for the electrochemical reconstruction of amorphous materials. Specifically, we revealed the dynamic mechanisms of the phase transitions, the heterogeneous interfaces, the electronic structures, and the correlations of the electrochemical characteristics of the CO₂RR. In the initial state, the a-In-SnO_x exhibited an unstable performance owing to the metastable structure of the amorphous materials. The current density and FE_{formate} exhibited increasing trends. In the activated state, the amorphous oxide partially nucleated and crystallised to form In-doped SnO₂ nanoparticles that further formed a/c-In-SnO₂, thus establishing an amorphous-crystalline heterostructure, which favoured the creation of active sites and enhanced the activity for the CO₂-to-formate conversion. Benefiting

from the heterostructure, the amorphous-crystalline In-doped SnO₂ (a/c-In-SnO₂) exhibited potential CO₂RR performance with a maximum Faraday efficiency of 94.6% at -1.0 V (vs. RHE). Moreover, the current densities of a/c-In-SnO₂ were approximately 90, 152, and 209 mA cm⁻² with the formate production rates of 4.43, 7.40, and 9.85 mmol m⁻² s⁻¹ at -1.0, -1.2, and -1.4 V (vs. RHE), respectively. In the deactivated state, the reduced metallic In-doped Sn exhibited poor activity in the CO₂RR owing to a considerably higher energy barrier. Furthermore, developing a targeted strategy to alleviate degradation during reconstruction is instructive. Finally, countermeasures and expectations were presented to inspire the rational design and optimisation of catalysts. This study reveals the dynamic structure–function relationship, provides a systematic understanding of the evolution mechanisms of amorphous materials, and proposes a feasible strategy for the in-situ reconstruction of amorphous-crystalline heterostructures for highly efficient CO₂ electroreduction.

2. Experimental section

2.1. Materials

KOH (95%), ethanol (>99.8%), InCl₃ (99.99%), glucose (AR) and isopropanol (99.5%) were all purchased from Shanghai Meryer Chemical Reagent Co., Ltd. SnCl₂·2 H₂O (98%), polyvinylpyrrolidone (MW 40 000, K30), ammonia solution (25%-28%), hydrazine hydrate (24%-26%) and thioacetamide (>98.0%) were purchased from Aladding Chemical Reagent Co., Ltd. Ethylene glycol (96%) was purchased from Tianjin Heowns Chemical Reagent Co., Ltd. Selenium powder (>99.99%) was purchased from Shanghai Macklin Chemical Reagent Co., Ltd. All reagents were used without any purification process. Ultra purity water (18.25 MΩ cm) supplied by a UP Water Purification System was used in the whole experimental processes. CO₂ (>99.999%) and Ar (>99.999%) were supplied by Air Liquid.

2.2. Material synthesis

The amorphous In doped SnO_x (a-In-SnO_x) was prepared via a solution chemical reduction method in a ice bath under an Ar atmosphere. First, 50 mg carbon quantum dots (CQDs) were dispersed into 50 mL ethanol to form the A solution. 2 mmol SnCl₂·2 H₂O and 0.02 mmol InCl₃ were dissolved in the ethanol to form B solution, which was kept in a ice bath with Ar atmosphere. Then the A solution was mixed into the B solution. After even agitation, ammonia solution was dropwise added into above mixed solution. After stirring for 12 h, the resulting solution was centrifuged at 10,000 rpm, the precipitates were collected and rinsed 3 times with deionized water and ethanol, respectively. Finally, the products were desiccated and calcined in a vacuum oven at 200 °C for 24 h. The CQDs were conveniently synthesized by anodic oxidation of alcohol according to the previous literature [24]. The crystalline In doped SnO₂ (c-In-SnO₂) was synthesized after calcine at 800 °C in an Ar atmosphere for 2 h. Similar to the above method for the In doped SnO₂, the crystalline SnO₂ (c-SnO₂) was synthesized without InCl₃ addition. For preparing amorphous SnSe (InSe), 1.5 mmol of SnCl₂·2 H₂O (InCl₃) was dissolved in ethylene glycol to marked as the solution A. On the other side, 1.5 mmol of selenium powder was added to 5 mL of hydrazine hydrate and stirred for 30 min, which marked as the solution B. Then, the solution B was slowly dropwise added into the solution A. The mix solution was then transferred to a 100 mL stainless steel Teflon-lined autoclave and heated to 100 °C for 12 h. Finally, the precipitates were collected by centrifugation and washed with deionized water. For preparing amorphous SnS, 1.0 g polyvinylpyrrolidone and 1.0 g glucose were dispersed into 60 mL ethylene glycol. When the solution is evenly mixed, 2 mmol SnCl₂·2 H₂O and 2 mmol thioacetamide were dissolved in the above solution. Then the obtained mixed solution was sealed in a Teflon-lined stainless steel autoclave and heated to 120 °C for 12 h. After cooling, the precipitates were collected by centrifugation and washed

with deionized water and ethanol.

2.3. Physicochemical and electrochemical characterization

X-ray diffraction (XRD) patterns of samples were acquired on a Bruker D8 Advanced diffractometer with a Cu K α source (40 KV and 40 mA) at the scan rate of 8° min $^{-1}$. The size and lattice fringes of the In-SnO $_x$ were characterized by scanning electronic microscopy (SEM) and transmission electron microscopy (TEM) on a JEOL JSM-7800 F and JEOL jem-2100 f with an EDX (200 kV), respectively. High-angle annular dark-field scanning transmission electron microscopy (HAADF-STEM) images were collected on a JEM-ARM200F. The operando Raman spectra were acquired with a laser excitation at 532 nm (HORIBA Lab RAM HR Evolution). The in-situ Raman measurements were performed via a flow-cell with three-electrode system, which was the same with our previous work [25]. The surface elemental compositions and chemical states were examined by X-ray photoelectron spectra (XPS, ESCALAB-250XI). The Fourier transform infrared (FTIR) spectra were carried out by using a Thermo Scientific Nicolet iS20 with the spectral range of 400–4000 cm $^{-1}$. Inductively coupled plasma optical emission spectrometry-optical emission spectrometer (ICP-OES) measurements were performed on an instrument of Agilent 725ES.

2.4. Electrochemical measurements in a Flow-Cell

CO $_2$ reduction was conducted in a custom-designed three-chamber flow cell, where aqueous KOH solution (1 M, pH=14) was used as the electrolytes, and a Ag/AgCl electrode (saturated KCl, Gaossunion) was employed as the reference electrode. CO $_2$ gas was supplied directly to the working electrode at a rate of 20 mL min $^{-1}$. A peristaltic pump (EC200-01) was used to control the flow rate of electrolytes at ~30 mL min $^{-1}$. The output of the gas flow from the cathode chamber was directed into a gas chromatograph instrument (GC20, Shanghai Ruimin Instrument Co., Ltd.). An activated Ni foam was used as the counter electrode. An anion exchange membrane (FAA-3-PK-130, Fumatech) was used to separate the cathode chamber and the anode chamber. The ink of catalysts were prepared by dispersing 20 mg of the a-In-SnO $_x$ and 20 μ L of Nafion Solution (5 wt%) in 750 μ L isopropyl alcohol and 230 μ L of ultra-purity water. After sonicated for 1 h, 50 μ L ink was added dropwise onto a gas diffusion layer (GDL). Electrolysis experiments were conducted using chronoamperometry with an electrochemical workstation (CH Instruments 660E). The gas products were analyzed by a gas chromatograph that equipped with a thermal conductivity detector (TCD) and flame ionization detector (FID). The liquid products were analyzed by using a nuclear magnetic resonance (NMR) instrument (AVANCE IIITM HD 400 MHz NanoBAY) and DMSO was added into the deuterated water solvent as an internal standard.

The faradaic efficiency of formate (FE_{formate}) can be calculated as Eq. (1):

$$FE_{formate} = \frac{2Fn}{Q} \quad (1)$$

where 2 is the number of electrons transferred in the electrochemical reaction, n is the amount of product (mol); F is the Faraday constant (96485 C·mol $^{-1}$), and Q represents the total charge consumed (C).

The formate production rate (r) represents their total amount produced per unit area of working electrode and unit of time. This figure of merit is defined by Eq. (2):

$$r(\text{mmol} \cdot \text{m}^{-2} \cdot \text{s}^{-1}) = \frac{n_m}{A} \quad (2)$$

where n_m is the number of moles of formate produced per unit of time (expressed in mmol·s $^{-1}$) and A is the geometric area of the cathode (m $^{-2}$).

2.5. Computational details

We employed the first principles to perform density functional theory (DFT) calculations within the generalized gradient approximation (GGA) using the Perdew-Burke-Ernzerhof (PBE) formulation [26–28]. We chose the projected augmented wave (PAW) potentials to describe the ionic cores and took valence electrons into account using a plane wave basis set with a kinetic energy cutoff of 450 eV [29,30]. Partial occupancies of the Kohn-Sham orbitals were allowed using the Gaussian smearing method and a width of 0.05 eV. The electronic energy was considered self-consistent when the energy change was smaller than 10 $^{-5}$ eV. A geometry optimization was considered convergent when the residual forces were smaller than 0.05 eV/Å. In addition, the PBE-D3 (IVDW = 11) dispersion term was introduced to correct the van der Waals interactions. The vacuum spacing in a direction perpendicular to the plane of the structure is 18 Å for the surfaces. The Brillouin zone integration was performed using 2×2×1 Monkhorst-Pack k-point sampling for a structure. Finally, the adsorption energies (E_{ads}) were calculated as E_{ads}= E_{ad/sub}-E_{ad}-E_{sub}, where E_{ad/sub}, E_{ad}, and E_{sub} are the total energies of the optimized adsorbate/substrate system, the adsorbate in the structure, and the clean substrate, respectively. The Gibbs reaction free energy change (ΔG) was calculated using the Eq. (3):

$$\Delta G = \Delta E + \Delta ZPE - T\Delta S \quad (3)$$

where ΔE is the reaction energy of the reactant and the product species adsorbed on the catalyst, which was directly obtained from DFT calculations; ΔZPE and ΔS are the changes in zero point energies and entropy at 298.15 K, which were calculated from the vibrational frequencies.

Ab initio molecular dynamics (AIMD) simulation was carried out to study disorder SnO $_2$ -structures. During geometry optimization, the cut-off energy was set as 400 eV for structures. The Monkhorst-Pack (MP) k-point grid of 1×1×1 point was used to sample the Brillouin zone of the supercell. In addition, the PBE-D3 dispersion term was also introduced to correct the van der Waals interactions. The Gaussian smearing methods (ISMEAR=0) was applied with a smearing width of 0.15 eV, and the convergence criteria for the energy and force were 10 $^{-4}$ eV and 0.05 eV/Å, respectively. The surface structure of SnO $_2$ was constructed where the surface contained the stoichiometric ratio structure of Sn₄₈O₉₆. The lattice parameter was 12.80×13.40×29.28. Sn elements were randomly replaced by 2 In atoms on the surface of SnO $_2$ to form the In-doped SnO $_2$ structure. According to the previous theoretical models of amorphous materials, the In-doped SnO $_2$ structure runs 10 ps kinetics at 300 K via AIMD simulations [17]. As the simulation time increases, the structure became amorphous with an atomic composition of In₂Sn₄₆O₉₆. After the simulation finishes, we further carried out the geometry optimizations to obtain the stabilized amorphous structure as the amorphous In-SnO $_x$.

3. Results and discussion

3.1. Design of highly active amorphous sample for CO $_2$ RR

Strategies of amorphous engineering and electrochemical activation were introduced to design the amorphous In-doped SnO $_x$ for optimising the CO $_2$ RR performance of tin oxides (Fig. 1a). The amorphous-crystalline In-doped SnO $_2$ (a/c-In-SnO $_2$) was synthesised via the electrochemical reconstruction during the CO $_2$ RR. As a basic material, amorphous In-doped SnO $_x$ (a-In-SnO $_x$) underwent restructuring and transformed into an amorphous-crystalline heterostructure during the operation. TEM (HR-TEM) images of a-In-SnO $_x$ and a/c-In-SnO $_2$ are shown in Fig. 1b and 1c, respectively. As shown in the Fig. 1b, no apparent lattice fringe was observed in the a-In-SnO $_x$. The atoms are disordered, and the selected-area electron diffraction (SAED) patterns show a wide diffraction ring, confirming the amorphous structure of the

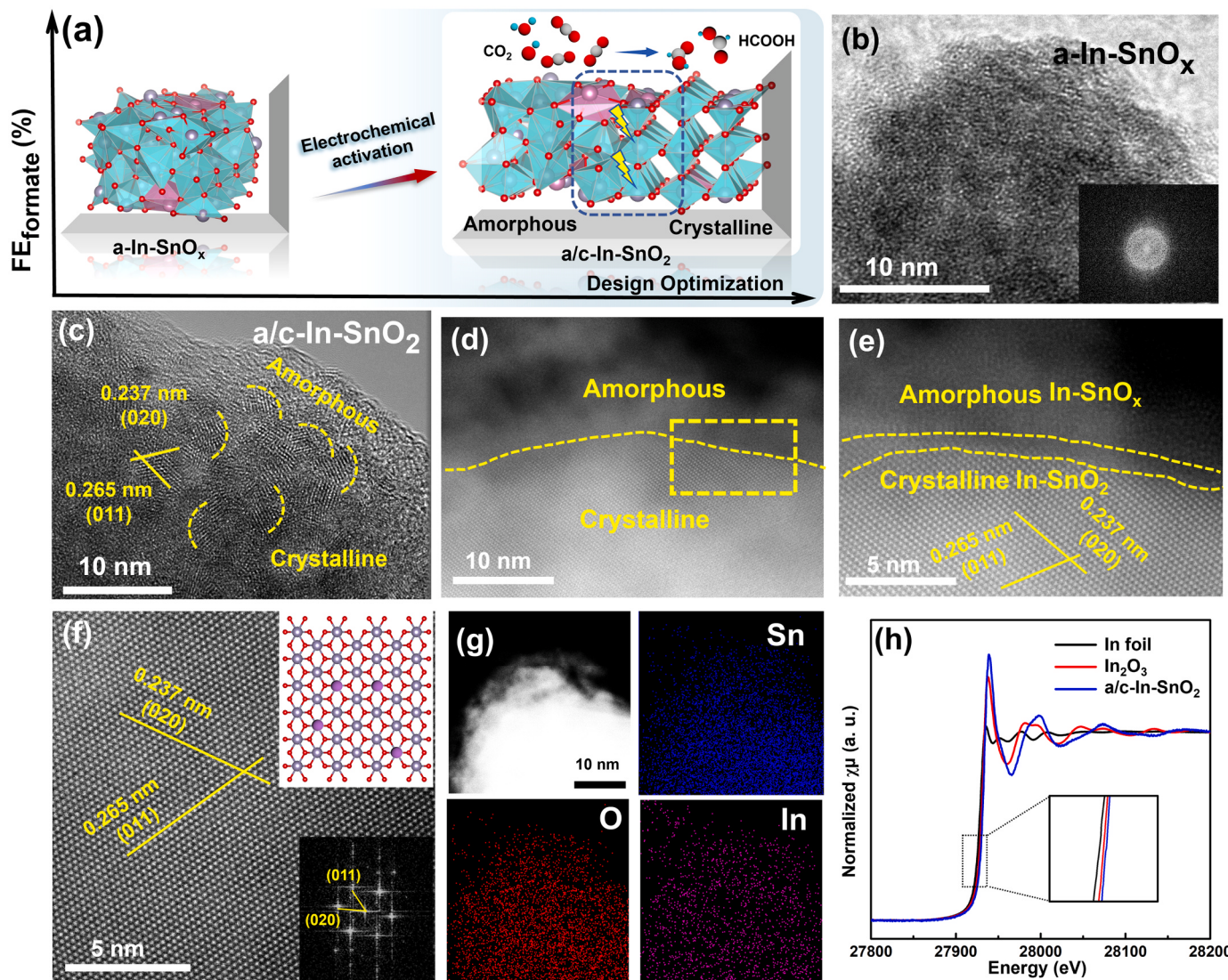


Fig. 1. (a) Schematic illustration of design optimization. The TEM images of (b) a-In-SnO_x and (c) a/c-In-SnO₂. (d, e, f) The HAADF-STEM images of a/c-In-SnO₂. (g) The HAADF-STEM elemental mappings of a/c-In-SnO₂. (h) In K-edge X-ray absorption near-edge structure (XANES) spectra.

material. After the electrochemical reconstruction, the a-In-SnO_x partially crystallised to form In-doped SnO₂ nanoparticles (Fig. 1c), establishing an amorphous–crystalline heterostructure interface. An atomic-resolution high-angle annular dark-field STEM (HAADF-STEM) analysis of the a/c-In-SnO₂ was performed to further identify the active state structure. As shown in Fig. 1d and e, the c-In-SnO₂ is coated by the amorphous In-doped SnO_x, with an apparent boundary presenting between the crystalline and amorphous phases.

The atoms in the crystalline structure were arranged regularly; as the atoms expanded outward, the atomic binding energy decreased, and the interatomic distance increased. When extended to the amorphous region, the atoms exhibited a disordered arrangement. In this boundary region, the arrangement of the atoms transitioned from a completely ordered state to a completely disordered state was different from traditional crystal and crystal heterostructure, where the arrangement of atoms transitions from an ordered arrangement to another ordered arrangement (Fig. 1e). As shown in Fig. 1f, the interplanar distances of 0.237 and 0.265 nm in the particle core were consistent with those of the (020) and (011) planes of tetrahedral SnO₂, respectively. Moreover, clear diffraction rings corresponding to the (020) and (011) crystalline planes of SnO₂ were observed in the SAED patterns. Furthermore, distinguishing In from Sn was difficult because of their relatively light

atomic masses. The elemental mappings demonstrate that In, O, and Sn are homogeneously distributed throughout the material (Fig. 1g). To further explore the occupation of the In, X-ray absorption fine structure spectroscopy (XAFS) was conducted. As shown in Fig. 1h, the values of the In K-edge of the a/c-In-SnO₂ was higher than that of standard In₂O₃, suggesting that the oxidation states of In in a/c-In-SnO₂ was higher than +3 [31,32]. Moreover, the In–O bond shifted to a lower radius distance in the Figure S1 [33,34]. These results could attribute to the modification of neighboring Sn⁴⁺ atoms in the environment. In addition, the formation energy of the substitution site of In also confirmed that the In was mainly to replace the Sn site on the surface (Figure S2). The sample compositions were determined using inductively coupled plasma optical emission spectrometry (ICP-OES), and the content of In atoms in a/c-In-SnO₂ was 6.78%.

3.2. Investigation of the *in-situ* formation of active amorphous–crystalline structure under the CO₂RR condition

To further explore the practical active sites of a/c-In-SnO₂ during the operation, potentiostatic measurements of amorphous SnO_x were performed in a CO₂RR flow cell at -1.0 V (vs. RHE) in the 1 M KOH electrolyte (Figure S3). As shown in Figs. 2a and 2b, the morphological

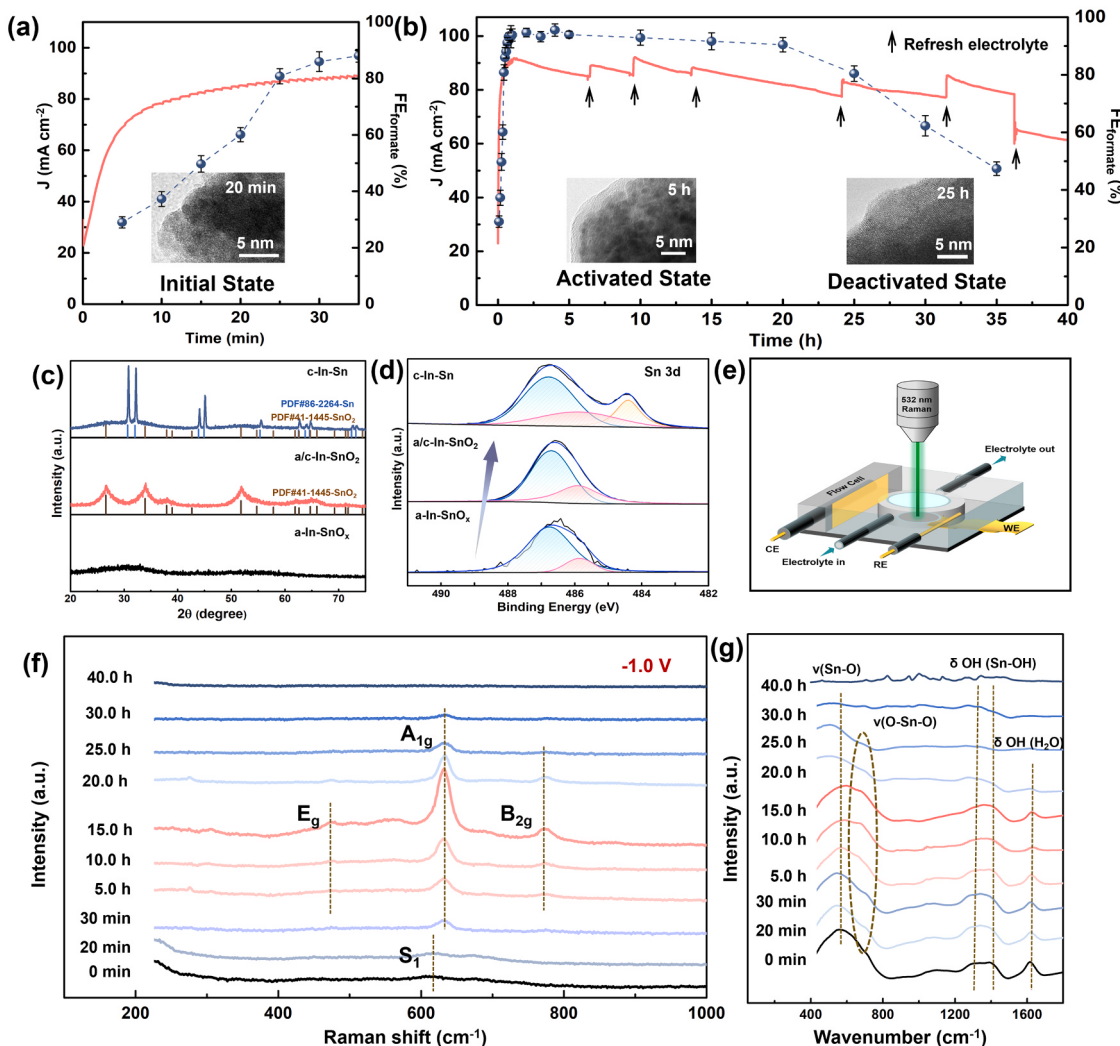


Fig. 2. (a, b) The current density and the Faradaic efficiencies of formate production of a-In-SnO_x. The corresponding (c) XRD patterns and (d) Sn 3d spectra of amorphous a-In-SnO_x, a/c-In-SnO₂, and c-In-Sn. (e) Schematic illustration of the in-situ Raman measurements performed via a flow-cell. (f) Raman spectra and (g) FTIR spectra of a-In-SnO_x during CO₂RR process.

characteristics and chemical performance underwent three reconstruction states: the initial state, activated state, and deactivated state. Additional TEM images and elemental mappings of a-In-SnO_x, a/c-In-SnO₂, and c-In-Sn are shown in Figure S4. At the initial state (0–0.5 h, Fig. 2a), a-In-SnO_x exhibited lower activity. However, the current density and the FE_{formate} gradually increased during the reconstruction process. In the second state, a-In-SnO_x reached an activated state (0.5–20 h), where a-In-SnO_x partially crystallised to form In-doped SnO₂ nanoparticles, establishing an amorphous-crystalline heterostructure interface (Fig. 2b). Moreover, a/c-In-SnO₂ achieved a FE_{formate} $\geq 90\%$ with a steady-state current density of $\sim 85 \text{ mA cm}^{-2}$ for 19 h. In the third state, a-In-SnO_x reached a deactivated state, where a/c-In-SnO₂ was gradually reduced to metallic In-doped Sn (denoted as c-In-Sn) and the FE_{formate} decreased to 47% after 35 h. Renewing the electrolyte (Figures S5 and S6) is necessary to ensure the consistency of the reaction environment. X-ray diffraction (XRD), X-ray photoelectron spectroscopy (XPS), Fourier-transform infrared spectroscopy (FTIR), and surface-enhanced Raman spectroscopy were employed to elucidate the processes and mechanisms of the amorphous reconstruction during the CO₂ electroreduction. As shown in the XRD patterns in Fig. 2c, a-In-SnO_x has an amorphous structure. During the CO₂RR, a visible phase change was observed in a/c-In-SnO₂. The broader diffraction peaks correspond to the planes of SnO₂ (JCPDS No. 41–1445). No other impurity peaks were

detected, suggesting the successful transformation of a-In-SnO_x into In-doped SnO₂ with low crystallinity. After long-term electroreduction, c-In-Sn exhibited sharp peaks corresponding to the planes of Sn (JCPDS No. 86–2264), confirming the transformation of the amorphous structure to In-doped SnO₂ and then to highly crystalline metallic In-doped Sn. XPS analysis was performed to evaluate the electronic structure of a-In-SnO_x. As shown in Fig. 2d, the XPS spectrum of Sn 3d showed that the content of the peak at $\sim 486.83 \text{ eV}$ (corresponding to Sn⁴⁺) decreased slightly in the activated state, demonstrating that the fraction of Sn⁴⁺ initially reduced to a lower binding energy [35]. In the deactivated state, the peak at $\sim 484.51 \text{ eV}$ (corresponding to Sn⁰) was observed in c-In-Sn, demonstrating metallic Sn generated under the reduction potential [36]. The content of Sn⁴⁺, Sn²⁺, and Sn⁰ in a-In-SnO_x, a/c-In-SnO₂, and c-In-Sn are listed in Table S1. In-situ surface-enhanced Raman spectroscopy of a-In-SnO_x was performed in a flow cell using a three-electrode system (Fig. 2e). Fig. 2f shows the Raman spectra of a-In-SnO_x during the reconstruction process at -1.0 V (vs. RHE). First, a-In-SnO_x exhibited a broad band (S1) in the low-frequency region of $\sim 610 \text{ cm}^{-1}$, resulting from its disordered structure and lattice distortion. As previously reported, the disordered arrangement and nanoparticle size strongly influence the vibrational properties. When the nanoparticle size decreases, the bands associated with the classical modes of SnO₂ shift and broaden according to the

phonon dispersion curves [37]. During operation, the classical modes of SnO_2 (E_g , A_{1g} , and B_{2g}) were detected in the activated state, implying the formation of In-doped SnO_2 nanoparticles in a/c-In-SnO_x [38]. In the deactivated state, the characteristic peaks of SnO_2 were attenuated and disappear, consistent with the transformation of metallic c-In-Sn. The FTIR studies of a-In-SnO_x were performed for different durations during the CO₂RR. As shown in Fig. 2g, the peaks at 562 and 669 cm^{-1} are assigned to terminal $\nu(\text{Sn}-\text{O})$ and $\nu(\text{O}-\text{Sn}-\text{O})$ stretching vibrations, respectively [39,40]. Furthermore, the peaks at 1290–1403 cm^{-1} and 1621 cm^{-1} are assigned to δOH (Sn-OH) and δOH (H_2O), respectively [41]. As the reaction progresses, the $\nu(\text{O}-\text{Sn}-\text{O})$ stretching vibrations increased in the activated state (a/c-In-SnO_x) and then decreased in the deactivated state (c-In-Sn). In contrast, the peak corresponding to $\nu(\text{Sn}-\text{O})$ was gradually flattened. These results can be attributed to the partial crystallisation of a-In-SnO_x into nanocrystalline In-doped SnO_2 , which subsequently reduces to metallic In-doped Sn. Brunauer–Emmett–Teller (BET) surface areas of a-In-SnO_x, a/c-In-SnO₂ and c-In-Sn were measured via N_2 isothermal adsorption and desorption. As shown in the Figure S7, the assessed BET surface areas of a-In-SnO_x, a/c-In-SnO₂ and c-In-Sn were 3.54 $\text{m}^2 \text{g}^{-1}$, 3.49 $\text{m}^2 \text{g}^{-1}$, 3.11 $\text{m}^2 \text{g}^{-1}$, respectively, indicating the morphological differences between these catalysts were negligible. The degree of crystallinity of c-In-Sn was also measured by differential scanning calorimetry (DSC) (Figure S8). All the above results reveal that a-In-SnO_x transformed to a/c-In-SnO₂ and then reduced to metallic c-In-Sn under CO₂RR operation, agreeing well with

the previous TEM and HAADF characterisation analyses. As previously reported, the cathodic potential or electronic field is assumed to be the driving force behind reconstruction [42–44]. In the first process (a-In-SnO_x→a/c-In-SnO₂), a-In-SnO_x partially crystallised to In-doped SnO_2 . Amorphous materials do not possess the long-range translational order characteristics of crystalline materials. The positively charged Sn vibrated towards the electrode, whereas the negatively charged O vibrated towards the opposite direction. This cross-vibration caused the sparse and disordered arrangement of atoms to become compact and ordered, thus forming oxide crystals with a short-range regular arrangement. In the second process (a/c-In-SnO₂→c-In-Sn), In-doped SnO_2 was reduced to metallic In-doped Sn. The driving force for this reconstruction was the cathodic potential. Oxides can be reduced to metals at a reduction potential over long periods of catalysis. This follows the general laws of thermodynamic theory [45]. In addition, material reconstruction under an Ar atmosphere exhibited a similar process (Figure S9).

3.3. Electrochemical properties of reconstructed a-In-SnO_x during CO₂RR

As previously mentioned, the a-In-SnO_x, a/c-In-SnO₂, and c-In-Sn electrodes were tested for the electrochemical properties in a flow cell (Fig. 3a). a/c-In-SnO₂ exhibited a significantly higher FE_{formate} (94.6%) than a-In-SnO_x (43.0%) and c-In-Sn (47.4%), revealing that a-In-SnO_x was activated to form a/c-In-SnO₂ and then deactivated to form c-In-Sn

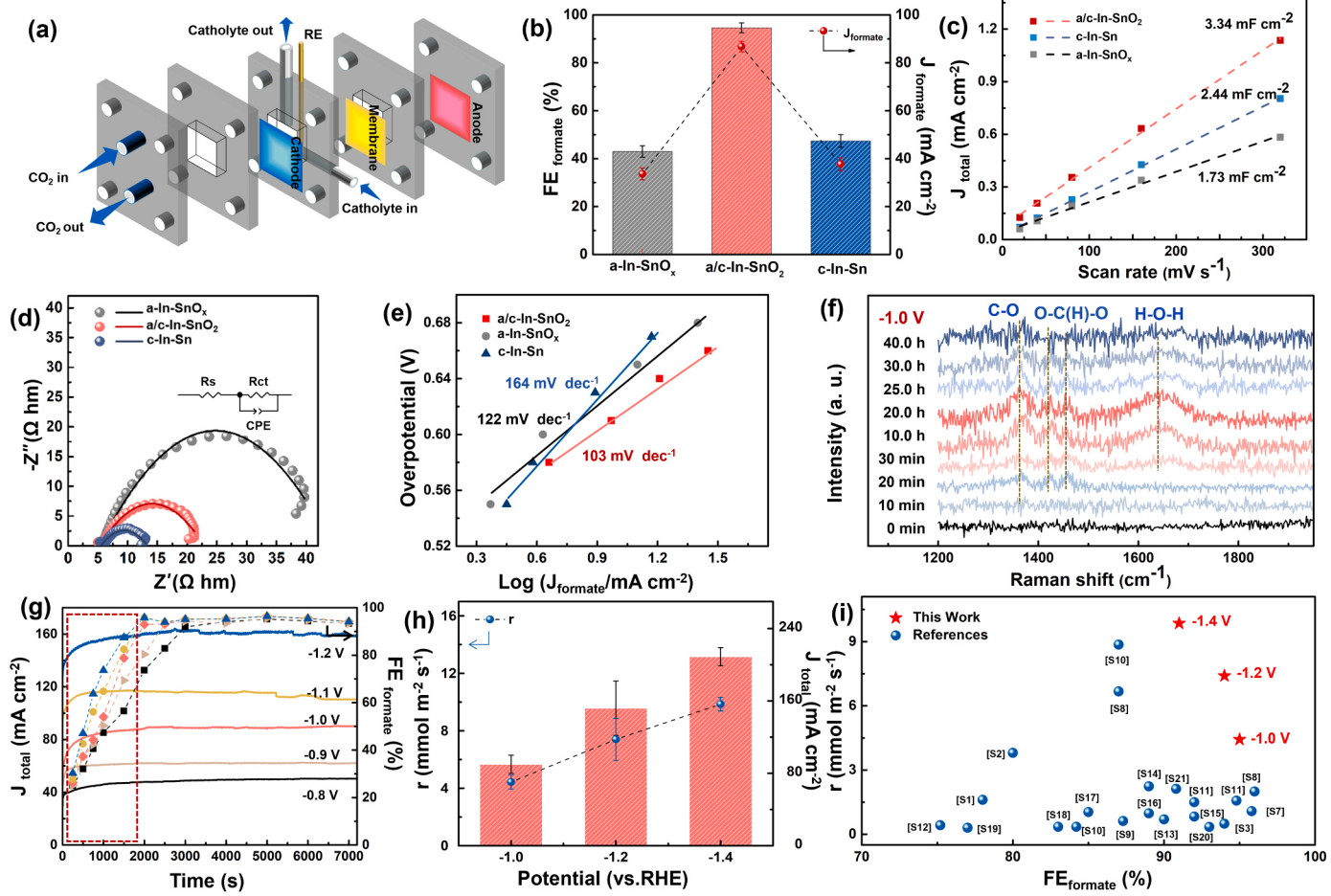


Fig. 3. (a) Schematic illustration of the flow cell configuration in this work, (b) Current density and FE_{formate} of the a-In-SnO_x, a/c-In-SnO₂, and c-In-Sn at -1.0 V (vs. RHE), (c) linear fitting of the capacitive current densities versus the scan rates, (d) Nyquist plots of the a-In-SnO_x, a/c-In-SnO₂, and c-In-Sn, (e) Tafel plots of formate product of a-In-SnO_x, a/c-In-SnO₂, and c-In-Sn, (f) In situ Raman spectroscopic study on the intermediate adsorption of a-In-SnO_x during the CO₂RR process. (g) The current density and (h) formate production rate (r) of a/c-In-SnO₂ at -1.0, -1.2, and -1.4 V (vs. RHE) potential (i) Previous literatures about SnO_x compounds catalysts for CO₂RR.

during the reconstruction process (Fig. 3b, S10, and S11). Linear sweep voltammetry (LSV) curves of a-In-SnO_x, a/c-In-SnO₂ and c-In-Sn were measured in a 1 M KOH electrolyte. As shown in Figure S12, a/c-In-SnO₂ exhibited a larger current density and more positive onset potential than that of a-In-SnO_x and c-In-Sn, suggesting a/c-In-SnO₂ facilitated CO₂ electroreduction. The double-layer capacitance (C_{dl}) was measured to evaluate the electrochemical surface area (ECSA) (Fig. 3c and S13). The C_{dl} of a-In-SnO_x was 1.73 mF cm⁻². As the CO₂RR progresses, the C_{dl} first increased to 3.34 mF cm⁻² for a/c-In-SnO₂, implying that the number of active sites increased in the activated state. Subsequently, the C_{dl} decreased to 2.44 mF cm⁻² for c-In-Sn, indicating that the number of active sites decreased in the deactivated state. The active sites were equipped with CO₂ and intermediate adsorption capacities that matched well with the FE_{formate}. Moreover, the ECSA-normalised formate current density is presented in the Figure S14, implying the intrinsic activity of samples. As shown in the Figure S14, the J_{formate} of a/c-In-SnO₂ increased substantially in the activated state, indicating that the activity of a/c-In-SnO₂ was optimized. And then, the J_{formate} of c-In-Sn decayed in the deactivated state, indicating reduction in the number of active sites for c-In-Sn. Electrochemical impedance spectroscopy further revealed the enhanced electron transfer capability of a-In-SnO_x, a/c-In-SnO₂, and c-In-Sn during the CO₂RR (Fig. 3d and Table S2). As shown in Fig. 3d, all curves were similar in shape to depressed semicircles, with the corresponding fitted circuit diagram presented in the illustration, where R_s is the ohmic resistance, R_{ct} is the charge-transfer impedance, and CPE is the depression of the semicircle. Compared to a-In-SnO_x (41.53 Ω), a/c-In-SnO₂ (21.73 Ω) exhibited small charge-transfer impedance values, demonstrating that the charge transfer rate of a/c-In-SnO₂ from the cathode surface to the CO₂^{*} species was faster than that of a-In-SnO_x. Owing to a large amount of metallic Sn, c-In-Sn exhibited a minimum impedance of 13.27 Ω. However, according to previous reports and the experimental results in Figure S15, unmodified metallic Sn has a specific selectivity for the hydrogen evolution reaction (HER), generally limiting its capacity for formate production [46,47]. Tafel slope analysis is a good approach for determining the rate-determining step (RDS) of the CO₂RR and analysing the reaction kinetics. As shown in Fig. 3e, the Tafel slopes of a-In-SnO_x, a/c-In-SnO₂, and c-In-Sn were approximately 118 mV dec⁻¹, suggesting that the reaction kinetics of the CO₂RR process was limited by the initial one-electron transfer step (* + CO₂ + e⁻ → CO₂^{*}) [48,49]. Moreover, the Tafel slope of 103 mV dec⁻¹ for a/c-In-SnO₂ was lower than those of c-In-Sn (122 mV dec⁻¹) and a-In-SnO_x (164 mV dec⁻¹), demonstrating that a/c-In-SnO₂ exhibited faster CO₂RR kinetics than c-In-Sn and a-In-SnO_x, possibly attributed to the formation of an abundant amorphous-crystalline interface heterojunction. These results indicate that activated a/c-In-SnO₂ has optimised reaction kinetics for formate after active reconstruction, consistent with the experimental observation that the activated a/c-In-SnO₂ achieves the highest FE_{formate} for the CO₂RR (Fig. 2a and b). We performed in-situ electrochemical Raman spectroscopy to monitor the reaction process and intermediate species of the CO₂RR (Fig. 3f). A double-band shape observed at 1420 and 1450 cm⁻¹ corresponding to an O-bound bidentate intermediate is ascribed to the key OCHO^{*} intermediate for formate product during the electro-reduction of CO₂ [48,50,51]. Notably, the intensities of these peaks gradually increased during 30 min of electrolysis.

This variation in the characteristic peaks intensity resulted from the increased number of active sites for the intermediate species, indicating that a-In-SnO_x was activated in the a/c-In-SnO₂ state. The C-O stretching peak at 1365 cm⁻¹ is assigned to HCOOH [48,52-54]. A broad peak located at ~1650 cm⁻¹ is attributed to the δ(H—O—H) vibrational peak of H₂O, indicating the participation of H₂O molecules during the CO₂RR process [55-57]. In addition, an apparent enhancement in the water peaks was observed for a/c-In-SnO₂, indicating a considerably enhanced water activation. The active *H species promote the formation of a crucial *OCHO intermediate [57]. This activated state was maintained for approximately 20 h, indicating that the number of surface-active

sites was maintained owing to the dynamic equilibrium of the catalytic structure. As the reaction time increased, the peaks associated with OCHO^{*} and HCOOH intermediates gradually decreased after 20 h, indicating that formate formation was almost completely suppressed. This result implies that the a/c-In-SnO₂ state is deactivated to the c-In-Sn state, consistent with the aforementioned experimental results. For comparison, the reconstruction process was monitored at different voltages. As shown in Fig. 3g and S16, as the applied voltage increased, the current density gradually increased. Simultaneously, the Faraday efficiency of formate reached its maximum value faster. These results demonstrate that a higher applied voltage accelerates the activation of the reconstruction process. Moreover, formate production rates (r) were measured at different applied potentials. As shown in Fig. 3h-i and Table S4, the current densities of a/c-In-SnO₂ were approximately 90 mA cm⁻², 152 mA cm⁻² and 209 mA cm⁻², and the formate production rates were 4.43 mmol m⁻² s⁻¹, 7.40 mmol m⁻² s⁻¹, and 9.85 mmol m⁻² s⁻¹ at -1.0 V, -1.2 V, and -1.4 V (vs. RHE), respectively. Both the selectivity and production rates of a/c-In-SnO₂ are prospective compared with previous reports about Sn-based catalysts for CO₂RR. These results adequately illustrate that a-In-SnO_x was activated in the a/c-In-SnO₂ state and then deactivated in the c-In-Sn state. During this reconstruction process, a/c-In-SnO₂ promoted the activity and selectivity of the CO₂RR. However, c-In-Sn was responsible for the long-term degradation. Accordingly, crystalline SnO₂ (c-SnO₂) and crystalline In-doped SnO₂ (c-In-SnO₂) were synthesised for comparison with a/c-In-SnO₂. The SEM and TEM images are shown in Figure S17. XRD patterns were performed to characterise the structure (Figure S18a), with c-SnO₂ and c-In-SnO₂ well-indexed to tetragonal SnO₂ (JCPDS No. 41-1445). c-SnO₂, c-In-SnO₂, and a/c-In-SnO_x electrodes were tested in a flow cell using 1.0 M KOH (pH=14) as the electrolyte. As shown in Figures S18b and S18c, a/c-In-SnO₂ delivers a significantly higher J_{formate} and FE_{formate} than c-In-SnO₂ and c-SnO₂. Especially, a/c-In-SnO₂ achieves the highest FE_{formate} of 94.6% at -1.0 V (vs. RHE). Consequently, compared with c-SnO₂ and c-In-SnO₂, a/c-In-SnO₂ exhibited significantly improved FE_{formate} after amorphous engineering and electrochemical activation. The effects of different In-doping amounts and electrolyte environment are discussed in the supporting information (Figure S19 and S20).

3.4. Theoretical calculation of reaction process and reconstructed model

DFT calculations were performed to elucidate the mechanisms of CO₂RR for formate and the activation and deactivation mechanisms of the entire reconstruction process. The structural models used for the DFT calculations are shown in Figures S21-S23. The Gibbs free energy diagrams for the CO₂-HCOOH conversion are shown in Figs. 4a and 4b, which show the free energy of each intermediate state and twice proton-coupled electron transfer. The theoretical overpotential for *OHCO on the a/c-In-SnO₂ heterostructure (0.59 eV) via the first proton-electron transfer reaction was lower than that of the a-In-SnO_x (0.80 eV), In-SnO₂ (1.06 eV), SnO₂ (1.25 eV), and c-In-Sn (1.56 eV) heterostructures (Fig. 4c). This difference indicated that the formation of the *OHCO intermediate in the former structure was thermodynamically more facile. a/c-In-SnO₂ exhibited the most favourable feasibility among all the investigated samples, corresponding to the high FE_{formate} in the activated state. This excellent selectivity may be attributed to the abundant amorphous-crystalline heterostructure, which can significantly decrease the free-energy barrier for HCOOH generation. Additionally, metallic In-doped Sn possessed the highest limiting potential among all the samples, suggesting that metallic In-doped Sn exhibited a lower feasibility for generating HCOOH. The Gibbs free energies of the HER process are shown in Figures S24 and S25. The energy barriers of the HER on a/c-In-SnO₂ were much higher than those on a-In-SnO_x and c-In-Sn, suggesting that the HER was preferable for c-In-Sn over a/c-In-SnO₂, corresponding to the deteriorative FE_{formate} of reduced c-In-Sn in the deactivated state. The binding energies of the intermediates were

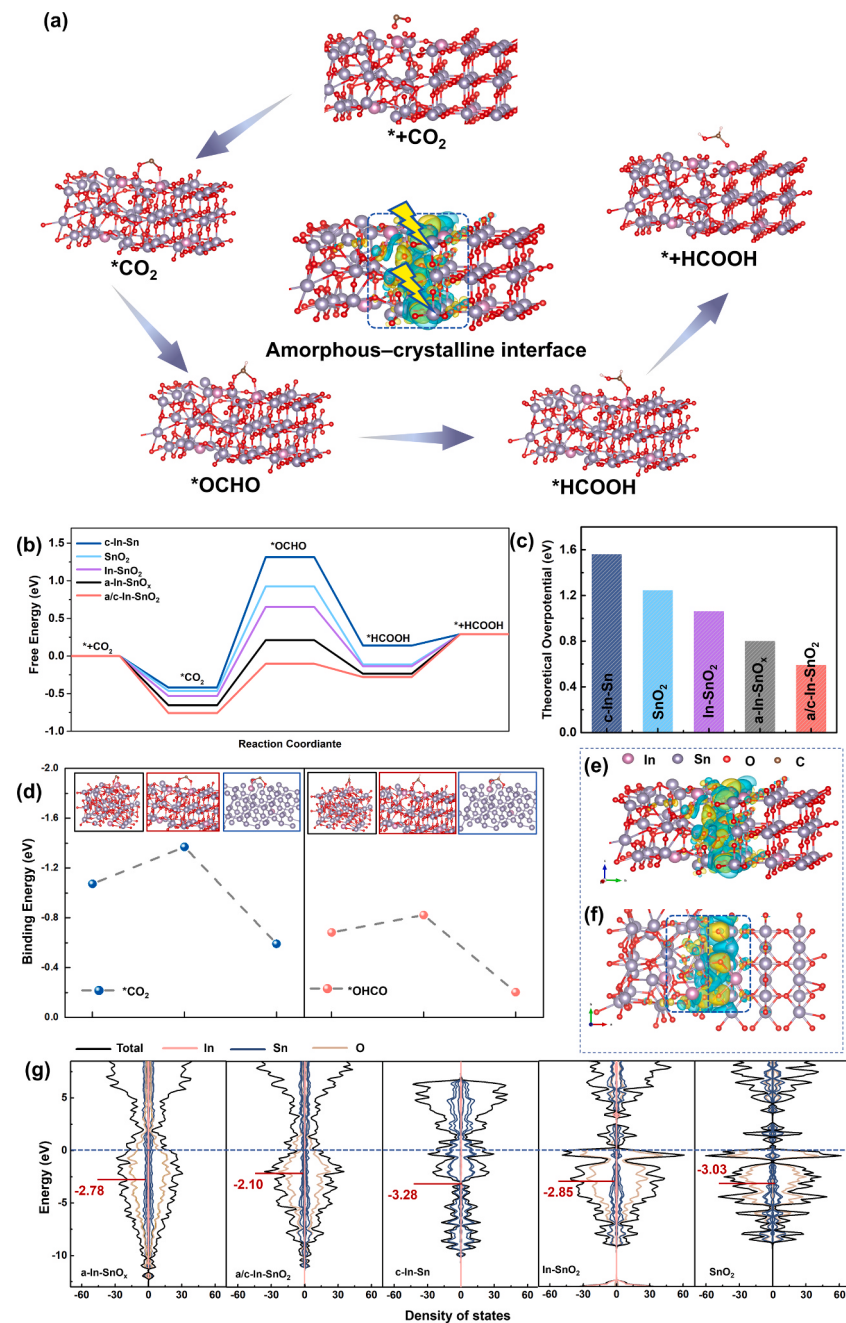


Fig. 4. (a) Schematic illustration of the CO₂RR process for formate. (b) Gibbs Free energy diagrams and (c) theoretical overpotential of a-In-SnO_x, a/c-In-SnO₂, c-In-Sn, SnO₂ and In-SnO₂. (d) Comparison of the binding energies of key intermediates for HCOOH production of a-In-SnO_x, a/c-In-SnO₂, and c-In-Sn. (e) Stereogram and (f) cross-section of charge density difference for a/c-In-SnO₂. (g) Projected DOS of a-In-SnO_x, a/c-In-SnO₂, c-In-Sn, SnO₂ and In-SnO₂. The vertical lines mark the positions of p-band center.

also calculated (Fig. 4d and S26). Compared with a-In-SnO_x and c-In-Sn, the activated a/c-In-SnO₂ exhibited optimised adsorption of *CO₂ and *OHCO, implying that the a/c-In-SnO₂ was the most conducive for CO₂→HCOOH conversion.

In contrast, the deactivated c-In-Sn delivered the weakest adsorption of *CO₂ and *OHCO, indicating that the catalytic sites for HCOOH were inactivated in the c-In-Sn state. As shown in Figs. 4e and 4f, in the crystalline In-doped SnO₂, Sn and In atoms tended to lose some of their electron densities and assumed positive valence states, whereas O atoms gathered electrons and assumed negative valence states. Compared with crystalline In-doped SnO₂, the distribution of electron clouds in a-In-doped SnO₂ was more complex because of its disordered atomic arrangement. Activated a/c-In-SnO₂ was spontaneously formed during

the reconstruction process and remained in a steady state. The amorphous–crystalline heterojunction with this specific electronic state was the critical active site for intermediate absorption/desorption during the CO₂RR. The projected density of states (DOS) were calculated to further understand the electronic structures of the samples (Fig. 4g). Compared to SnO₂, In-doped SnO₂ presented an apparent up-shifted electronic state, revealing that In-doping improved the adsorption of intermediates, which was available to optimise the activity of the CO₂RR, consistent with the binding energy results. Therefore, In-doping is a strategy for modulating the electronic structures of formate products. Compared to In-SnO₂, the p-band centre of a-In-SnO_x shifted from -2.85 eV to -2.78 eV, possibly attributed to the abundant defects of amorphous material. Moreover, when partial a-In-SnO_x crystallises to

form a/c-In-SnO₂, the p-band centre shifted up significantly to -2.10 eV, possibly owing to the specific electronic structure of the amorphous–crystalline heterostructure. Benefiting from the modulated electronic structures, the activated a/c-In-SnO₂ exhibited optimal activity for formate conversion. Moreover, in the deactivated state, the DOS of c-In-Sn exhibited a lower p-band centre (-3.28 eV), indicating weak adsorption of key intermediates. Consequently, the weakened $^*\text{CO}_2$ and $^*\text{OHCO}$ adsorption significantly inhibited the CO₂RR. Therefore, the calculations illustrated that the amorphous–crystalline heterostructure was the key to increasing the CO₂RR activity of a/c-In-SnO₂. During the CO₂RR, a-In-SnO_x was spontaneously activated to a/c-In-SnO₂, establishing the amorphous–crystalline heterostructure. An increased active surface area in the activated state promoted formate selectivity. However, in the deactivated state, a/c-In-SnO₂ was reduced to metallic c-In-Sn, which exhibited poor activity for the CO₂RR owing to its dynamic energy barrier. These results reveal that the critical active site of the activated a/c-In-SnO₂ was the amorphous–crystalline heterostructure, and the failure mechanism of deactivated c-In-Sn was the competing HER caused by metallic Sn during CO₂RR electrocatalysis.

3.5. Universal reconstruction mechanism for amorphous materials during CO₂RR

We prepared a series of amorphous materials (including metal oxides, sulfides, and selenides) to verify the universality of the reconstruction process during CO₂RR. Amorphous SnO_x, SnS_x, SnSe_x, InO_x, and InSe_x were also prepared to explore the reconstruction behaviour during the CO₂RR (Figures S27–S29). As shown in Figure S27, the amorphous SnO_x exhibited improved stability and activity, indicating that the influence of In-doping on the reconstruction process and failure mechanism was practical significant in the design of active catalysts. More importantly, all amorphous materials exhibited similar reconfiguration behaviours (Figures S28 and S29). In their initial state, amorphous materials exhibited a disordered atomic arrangement. In the second state, the amorphous materials partially crystallised to form Sn (In)O(S/Se)_x nanoparticles and established amorphous–crystalline heterostructure interface. In the third state, the crystalline Sn(In)O(S/Se)_x was gradually reduced to metallic Sn(In) nanoparticles. Therefore, the reconstruction of amorphous materials is universal during the CO₂RR process. Although the overall trend was consistent, the rate of amorphous material evolution is different. The evolution mechanism may be related to the structure of the amorphous material, including its phase structure, bond strength, and coordination environment. Besides the In atom, other elements can also be used to modify amorphous SnO_x, such as Cu and Zn. As shown in Figure S30, the amorphous a-Cu-SnO_x and a-Zn-SnO_x exhibited similar reconfiguration behaviours. Therefore, these results provide a universal regulation for the reconstruction of amorphous catalysts, which has important scientific significance in understanding the catalytic characteristics of amorphous catalysts and exploring their practical active structures. In addition, the following three suggestions can be used as references for the fabrication of materials: 1) Synthesis of a composite material with an auxiliary carrier to absorb electrons and protect the active oxide layer from self-reduction [57,58]. The premise is that the catalytic activity of this material is not affected during the reduction process. 2) Synthesis of core–shell structured catalysts with highly conductive metal cores and thin metal-oxide shells [59]. A homogeneous metal core with the desired stoichiometric ratio is used to stabilise the outer shell. The catalytic shell structure cannot be reconstructed during the CO₂RR process; 3) Triggering the emergence of oxygen vacancies in the SnO₂ lattice via atom doping and carrier reconstruction to stabilize the oxidation state of SnO₂ during the CO₂RR [48]. The cocatalyst could further oxidise metallic Sn during dynamic reconstruction. Hence, we synthesised a-In-SnO_x/C composite material with activated carbon as the support material to avoid this inevitable deactivation. Benefiting from its electrical conductivity and high dispersion area, the carbon support structure could

inhibit grain reduction and growth caused by electron aggregation. As shown in Figures S31 and S32, the a-In-SnO_x/C exhibited a long-term stability over 35 h and achieved a nearly 90% formate selectivity at -1.0 V vs. RHE.

4. Conclusion

In this study, amorphous In-doped SnO_x was selected as the basic material for the in-situ formation of a/c-In-SnO₂ during CO₂RR reconstruction. During CO₂RR reconstruction, a-In-SnO_x partially crystallised to In-doped SnO₂, forming an amorphous–crystalline interface for the activated a/c-In-SnO₂. This spontaneous reconstruction significantly favours charge transfer during the electrochemical process and enhances the adsorption of CO_2^* and OCHO^* intermediates, leading to improving selectivity for the CO₂RR. The entire reconstruction process was divided into three states: initial (a-In-SnO_x), activated (a/c-In-SnO₂), and deactivated (c-In-Sn). After summarising the reconstruction processes of different amorphous materials, we found that all amorphous materials exhibited similar reconfiguration behaviours. These results provide a universal regularity for reconstructing amorphous catalysts during the CO₂RR. This work establishes a dynamic correlation between the restructured structure and the catalytic performance of Sn oxide in various states during long-term electrocatalysis and provides insights into the evolution and failure mechanisms of amorphous Sn oxide materials, potentially inspiring the rational design and optimisation of CO₂RR electrocatalysts.

CRediT authorship contribution statement

Jun Zhao: Investigation. **Jinfeng Zhang:** Visualization, Resources. **Xixi Ren:** Investigation. **Han Wu:** Investigation. **Fei Liu:** Writing – original draft, Visualization, Methodology, Investigation, Formal analysis, Data curation, Conceptualization. **Jiajun Wang:** Writing – review & editing. **Yida Deng:** Writing – review & editing. **Wenbin Hu:** Resources. **Xiaopeng Han:** Writing – review & editing. **Wei Xie:** Resources. **Guangjin Wang:** Data curation.

Declaration of Competing Interest

The authors declare that they have no known competing financial interests or personal relationships that could have appeared to influence the work reported in this paper.

Data Availability

Data will be made available on request.

Acknowledgements

This work was supported by grants from the National Natural Science Foundation of China (Grants No. 52231008, 52372217, 52122107), Natural Science Foundation of Tianjin (Grants No. 22JCQNJC00830) and Guangdong Provincial and Municipal Joint Foundation for Basic and Applied Basic Research (Grants No. 2023A1515140180).

Appendix A. Supporting information

Supplementary data associated with this article can be found in the online version at doi:10.1016/j.apcatb.2024.124004.

References

[1] W. Zheng, X. Yang, Z. Li, B. Yang, Q. Zhang, L. Lei, Y. Hou, Designs of tandem catalysts and cascade catalytic systems for CO₂ upgrading, *Angew. Chem. Int. Ed.* 62 (2023) e202307283.

[2] J. Chen, D. Wang, X. Yang, W. Cui, X. Sang, Z. Zhao, L. Wang, Z. Li, Accelerated transfer and spillover of carbon monoxide through tandem catalysis for kinetics-boosted ethylene electrosynthesis, *Angew. Chem. Int. Ed.* 62 (2023) e202215406.

[3] X. Peng, L. Zeng, D. Wang, Z. Liu, Y. Li, Z. Li, B. Yang, L. Lei, L. Dai, Y. Hou, Electrochemical C–N coupling of CO₂ and nitrogenous small molecules for the electrosynthesis of organonitrogen compounds, *Chem. Soc. Rev.* 52 (2023) 2193–2237.

[4] C. Shen, X.-Y. Meng, R. Zou, K. Sun, Q. Wu, Y.-X. Pan, C.-J. Liu, Boosted sacrificial-agent-free selective photoreduction of CO₂ to CH₃OH by rhodium atomically dispersed on indium oxide, *Angew. Chem. Int. Ed.* (2024) e202402369.

[5] N. Li, P. Yan, Y. Tang, J. Wang, X. Yu, H. Wu, In-situ formation of ligand-stabilized bismuth nanosheets for efficient CO₂ conversion, *Appl. Catal. B-Environ.* 297 (2021) 120481.

[6] G. Liu, Z. Li, J. Shi, Y. Qiu, Y. Liu, Z. Wang, P. Hua, Black reduced porous SnO₂ nanosheets for CO₂ electroreduction with high formate selectivity and low overpotential, *Appl. Catal. B-Environ.* 260 (2020) 118134.

[7] S. Liu, J. Xiao, X. Lu, J. Wang, X. Wang, X. Lou, Efficient electrochemical reduction of CO₂ to HCOOH over sub-2 nm SnO₂ quantum wires with exposed grain boundaries, *Angew. Chem. Int. Ed.* 58 (2019) 8499–8503.

[8] Q. Chang, Y. Liu, J.H. Lee, D. Ologunoba, S. Hwang, Z. Xie, J.G. Chen, Metal-coordinated phthalocyanines as platform molecules for understanding isolated metal sites in the electrochemical reduction of CO₂, *J. Am. Chem. Soc.* 144 (2022) 16131–16138.

[9] H. Li, H. Du, H. Luo, H. Wang, W. Zhu, Y. Zhou, Recent developments in metal nanocluster-based catalysts for improving photocatalytic CO₂ reduction performance, *Microstructures* 3 (2023) 2023024.

[10] A.D. Handoko, F. Wei, Jenndy, B.S. Yeo, Z.W. Seh, Understanding heterogeneous electrocatalytic carbon dioxide reduction through operando techniques, *Nat. Catal.* 1 (2018) 922–934.

[11] J. Wang, X. Zheng, G. Wang, Y. Cao, W. Ding, J. Zhang, H. Wu, J. Ding, H. Hu, X. Han, T. Ma, Y. Deng, W. Hu, Defective bimetallic selenides for selective CO₂ electroreduction to CO, *Adv. Mater.* 34 (2022) 2106354.

[12] X. Ren, F. Liu, H. Wu, Q. Lu, J. Zhao, Y. Liu, J. Zhang, J. Mao, J. Wang, X. Han, Y. Deng, W. Hu, Reconstructed bismuth oxide through in situ carbonation by carbonate-containing electrolyte for highly active electrocatalytic CO₂ reduction to formate, *Angew. Chem. Int. Ed.* 63 (2024) e202316640.

[13] X. Zhao, Y. Wang, L. Zhan, M. Liu, J. Wu, D. Deng, J. Jiang, X. Zheng, Enhanced electron transfer by In doping in SnO_x for efficient CO₂ electroreduction to C₁ products, *Chem. Commun.* 58 (2022) 12716–12719.

[14] S. Chang, Y. Xuan, Q. Wang, K. Wang, Bimetallic In-Sn core-shell catalyst enabling highly efficient electrocatalytic CO₂ reduction to formate, *ACS Appl. Eng. Mater.* 1 (2023) 1514–1523.

[15] S. Ning, J. Wang, S. Huang, W. Chen, S. Chen, Electrochemical reduction of SnO₂ to Sn from the bottom: in-situ formation of SnO₂/Sn heterostructure for highly efficient electrochemical reduction of carbon dioxide to formate, *J. Catal.* 399 (2021) 67–74.

[16] H. Han, S. Jin, S. Park, Y. Kim, D. Jang, M.H. Seo, W.B. Kim, Plasma-induced oxygen vacancies in amorphous MnO_x boost catalytic performance for electrochemical CO₂ reduction, *Nano Energy* 79 (2021) 105492.

[17] S. Liu, S. Geng, L. Li, Y. Zhang, G. Ren, B. Huang, Z. Hu, J.F. Lee, Y.H. Lai, Y. H. Chu, Y. Xu, Q. Shao, X. Huang, A top-down strategy for amorphization of hydroxyl compounds for electrocatalytic oxygen evolution, *Nat. Commun.* 13 (2022) 1187.

[18] N. Yang, H. Cheng, X. Liu, Q. Yun, Y. Chen, B. Li, B. Chen, Amorphous/crystalline hetero-phase Pd nanosheets: one-pot synthesis and highly selective hydrogenation reaction, *Adv. Mater.* 30 (2018) 1803234.

[19] S. Shen, Z. Wang, Z. Lin, K. Song, Q. Zhang, Crystalline-amorphous interfaces coupling of CoSe₂/CoP with optimized d-band center and boosted electrocatalytic hydrogen evolution, *Adv. Mater.* 34 (2022) 2110631.

[20] B. Jia, B. Zhang, Z. Cai, X. Yang, L. Li, L. Guo, Construction of amorphous/crystalline heterointerfaces for enhanced electrochemical processes, *eScience* (2023) 100112.

[21] X. Li, S. Wang, L. Li, Y. Sun, Y. Xie, Progress and perspective for in situ Studies of CO₂ reduction, *J. Am. Chem. Soc.* 142 (2020) 9567–9581.

[22] Z. Han, D. Han, Z. Chen, J. Gao, G. Jiang, X. Wang, S. Lyu, Y. Guo, C. Geng, L. Yin, Steering surface reconstruction of copper with electrolyte additives for CO₂ electroreduction, *Nat. Commun.* 13 (2022) 3158.

[23] J. Chen, L. Wang, Effects of the catalyst dynamic changes and influence of the reaction environment on the performance of electrochemical CO (2) reduction, *Adv. Mater.* 34 (2022) 2103900.

[24] J. Deng, Q. Lu, N. Mi, H. Li, M. Liu, M. Xu, L. Tan, Q. Xie, Y. Zhang, S. Yao, Electrochemical synthesis of carbon nanodots directly from alcohols, *Chem. Eur. J.* 20 (2014) 4993–4999.

[25] F. Liu, X. Ren, J. Zhao, H. Wu, J. Wang, X. Han, Y. Deng, W. Hu, Inhibiting sulfur dissolution and enhancing activity of SnS for CO₂ electroreduction via electronic state modulation, *ACS Catal.* 12 (2022) 13533–13541.

[26] F.J. Kresse G, Efficient iterative schemes for ab initio total-energy calculations using a plane-wave basis set, *Phys. Rev. B* 54 (1996) 11169.

[27] F.J. Kresse G, Efficiency of ab-initio total energy calculations for metals and semiconductors using a plane-wave basis set, *Comp. Mater. Sci.* 6 (1996) 15–50.

[28] J.P. Perdew, Burke, K. Ernzerhof, Generalized gradient approximation made simple, *Phys. Rev. Lett.* 77 (1996) 3865–3868.

[29] G. Kresse, D. Joubert, From ultrasoft pseudopotentials to the projector augmented-wave method, *Phys. Rev. B* 59 (1999) 1758.

[30] P.E. Blöchl, Projector augmented-wave method, *Phys. Rev. B* 50 (1994) 17953.

[31] H. Min, D. Lee, J. Kim, G. Kim, K. Lee, J. Kim, M. Paik, Perovskite solar cells with atomically coherent interlayers on SnO₂ electrodes, *Nature* 598 (2021) 444–450.

[32] O. Erken, O. Ozkendir, M. Gunes, E. Harputlu, A study of the electronic and physical properties of SnO₂ thin films as a function of substrate temperature, *Ceram. Int.* 45 (2019) 19086–19092.

[33] E. Zhang, L. Tao, J. An, J. Zhang, L. Meng, X. Zheng, Engineering the local atomic environments of indium single-atom catalysts for efficient electrochemical production of hydrogen peroxide, *Angew. Chem. Int. Ed.* 134 (2022) 202117347.

[34] X. Liu, Y. Xie, M. Hao, Z. Chen, H. Yang, Highly efficient electrocatalytic uranium extraction from seawater over an amidoxime-functionalized In-N-C catalyst, *Adv. Sci.* 9 (2022) 2201735.

[35] Z. Chen, M.-R. Gao, N. Duan, J. Zhang, Y.-Q. Zhang, T. Fan, J. Zhang, Y. Dong, J. Li, Q. Liu, X. Yi, J.-L. Luo, Tuning adsorption strength of CO₂ and its intermediates on tin oxide-based electrocatalyst for efficient CO₂ reduction towards carbonaceous products, *Appl. Catal. B-Environ.* 277 (2020) 119252.

[36] K. Balakrishnan, J. Schwank, A chemisorption and XPS study of bimetallic Pt-Sn/Al₂O₃ catalysts, *J. Catal.* 127 (1991) 287–306.

[37] A. Diéguez, A. Romano-Rodríguez, A. Vilà, J.R. Morante, The complete Raman spectrum of nanometric SnO₂ particles, *J. Appl. Phys.* 90 (2001) 1550–1557.

[38] S. Das, S. Kar, S. Chaudhuri, Optical properties of SnO₂ nanoparticles and nanorods synthesized by solvothermal process, *J. Appl. Phys.* 99 (2006) 114303.

[39] B.-V.F. Amalric-Popescu D, Infrared studies on SnO₂ and Pd/SnO₂, *Catal. Today* 70 (2001) 1–3.

[40] A.F. Khan, M. Mehmood, M. Aslam, M. Ashraf, Characteristics of electron beam evaporated nanocrystalline SnO₂ thin films annealed in air, *Appl. Surf. Sci.* 256 (2010) 2252–2258.

[41] H. Wang, F. Sun, Y. Zhan, L. Li, H. Che, Q. Wu, J. Yu, Photochemical growth of nanoporous SnO₂ at the air–water interface and its high photocatalytic activity, *J. Mater. Chem. B* 20 (2010) 5641–5645.

[42] V.H.V. Quy, I.-R. Jo, S.-H. Kang, K.-S. Ahn, Amorphous-crystalline dual phase WO₃ synthesized by pulsed-voltage electrodeposition and its application to electrochromic devices, *J. Ind. Eng. Chem.* 94 (2021) 264.

[43] S.S. Djokić, Electrodeposition of amorphous alloys based on the iron group of metals, *J. Electrochem. Soc.* 146 (1999) 1824.

[44] X. Li, Y. Wang, J. Wang, Y. Da, J. Zhang, L. Li, C. Zhong, Y. Deng, X. Han, W. Hu, Sequential electrodeposition of bifunctional catalytically active structures in MoO₃/Ni–NiO composite electrocatalysts for selective hydrogen and oxygen evolution, *Adv. Mater.* 32 (2020) 2003414.

[45] A. Dutta, A. Kuzume, M. Rahaman, S. Vesztergom, P. Broekmann, Monitoring the chemical state of catalysts for CO₂ electroreduction: an in-operando study, *ACS Catal.* 5 (2015) 7498–7502.

[46] Y. Jiang, J. Shan, P. Wang, L. Huang, Y. Zheng, S.-Z. Qiao, Stabilizing oxidation state of SnO₂ for highly selective CO₂ electroreduction to formate at large current densities, *ACS Catal.* 13 (2023) 3101–3108.

[47] Y. Cheng, J. Hou, P. Kang, Integrated capture and electroreduction of flue gas CO₂ to formate using amine functionalized SnO_x nanoparticles, *ACS Energy Lett.* 6 (2021) 3352–3358.

[48] P. Deng, H. Wang, R. Qi, J. Zhu, S. Chen, F. Yang, L. Zhou, K. Qi, H. Liu, B.Y. Xia, Bismuth oxides with enhanced bismuth–oxygen structure for efficient electrochemical reduction of carbon dioxide to formate, *ACS Catal.* 10 (2019) 743–750.

[49] Z. Zhang, F. Ahmad, W. Zhao, W. Yan, W. Zhang, H. Huang, C. Ma, J. Zeng, Enhanced electrocatalytic reduction of CO₂ via chemical coupling between indium oxide and reduced graphene oxide, *Nano Lett.* 19 (2019) 4029–4034.

[50] D. Bohra, I. Ledezma-Yanez, G. Li, W. Jong, E.A. Pidko, W. Smith, Lateral adsorbate interactions inhibit HCOO[–] while promoting CO selectivity for CO₂ electrocatalysis on silver, *Angew. Chem. Int. Ed.* 131 (2019) 1359–1363.

[51] S. Kai, W. Chaozhi, X. Guangzhi, Surface enhanced raman spectra of carbonate, hydrocarbonate, and substituted acetic acids on silver hydrosols, *Spectrochim. Acta A* 45 (1989) 1029–1032.

[52] R.J. Madix, S.W. Jorgensen, Active oxygen on group VIII metals: activation of formic acid and formaldehyde on Pd (100), *J. Am. Chem. Soc.* 110 (1988) 397–400.

[53] A. Yamakata, J. Kubota, J.N. Kondo, K. Domen, C. Hirose, Isotope exchange reaction of formate with molecular hydrogen on Ni (110) by IRAS, *J. Phys. Chem. C* 100 (1996) 18177–18182.

[54] A. Miki, S. Ye, M. Osawa, Surface-enhanced IR absorption on platinum nanoparticles: an application to real-time monitoring of electrocatalytic reactions, *Chem. Commun.* 14 (2002) 1500–1501.

[55] B. Yang, L. Chen, S. Xue, H. Sun, K. Feng, Y. Chen, X. Zhang, L. Xiao, Y. Qin, J. Zhong, Z. Deng, Y. Jiao, Y. Peng, Electrocatalytic CO₂ reduction to alcohols by modulating the molecular geometry and Cu coordination in bicentric copper complexes, *Nat. Commun.* 13 (2022) 5122.

[56] G. Zhang, Z.J. Zhao, D. Cheng, H. Li, J. Yu, Q. Wang, H. Gao, J. Guo, H. Wang, G. A. Ozin, T. Wang, J. Gong, Efficient CO₂ electroreduction on facet-selective copper films with high conversion rate, *Nat. Commun.* 12 (2021) 5745.

[57] H. Liu, B. Li, Z. Liu, Z. Liang, H. Chuai, H. Wang, S.N. Lou, Y. Su, S. Zhang, X. Ma, Ceria-mediated dynamic Sn⁴⁺/Sn⁶⁺ redox cycle for CO₂ electroreduction, *ACS Catal.* 13 (2023) 5033–5042.

[58] J. Duan, T. Liu, Y. Zhao, R. Yang, Y. Zhao, W. Wang, Y. Liu, H. Li, Y. Li, T. Zhai, Active and conductive layer stacked superlattices for highly selective CO₂ electroreduction, *Nat. Commun.* 13 (2022) 2039.

[59] K. Ye, Z. Zhou, J. Shao, L. Lin, D. Gao, N. Ta, R. Si, G. Wang, X. Bao, In situ reconstruction of a hierarchical Sn-Cu/SnO_x core/shell catalyst for high-performance CO₂ electroreduction, *Angew. Chem. Int. Ed.* 59 (2020) 4814–4821.